Analytical Modeling of Silicon Microring and Microdisk Modulators With Electrical and Optical Dynamics

Raphaël Dubé-Demers, Jonathan St-Yves, Antoine Bois, Qiuhang Zhong, Michael Caverley, Yun Wang, Lukas Chrostowski, Sophie LaRochelle, David V. Plant, and Wei Shi

Analytical Modeling of Silicon Microring and Microdisk Modulators with Electrical and Optical Dynamics

Raphaël Dubé-Demers, Jonathan St-Yves, Antoine Bois, *Student Member, OSA*, Qiuhang Zhong,
Michael Caverley, *Student Member, IEEE, Student Member, OSA*,
Yun Wang, *Student Member, IEEE, Student Member, OSA*, Lukas Chrostowski,
Sophie LaRochelle, *Senior Member, IEEE, Fellow, OSA*, David V. Plant, *Fellow, OSA* and
Wei Shi, *Member, IEEE*

Abstract—We propose an analytical, time domain model for microring and microdisk modulators which considers both their electrical and optical properties. Theory of the dynamics of microring/microdisk is discussed, and general solutions to the transfer matrix representation are presented. Both static and dynamic predictions from the model are compared to measurement results to demonstrate the accuracy of our model. Static predictions and measurements are presented for power and phase responses whereas dynamic predictions and measurements are presented for small-signal and large-signal operations. The model verifies that the chirping and modulation bandwidth of the modulators depend on the detuning state. Finally, the accuracy and scalability of several techniques employed in the model are discussed.

Index Terms—Optical modulator, Silicon-on-insulator, Integrated optics, Electro-optic modulation, Optical resonators, Ring resonators, Disk resonators

I. INTRODUCTION

SILICON microring/microdisk modulators are an advantageous technology due to their ultra-compact footprint and high modulation efficiency. They have great potential for high-speed interconnects [1] and coherent transmission systems [2]. The development of such technology relies on our understanding in electrooptics, and with that arises the need for systematic engineering. In

R. Dubé-Demers, J. St-Yves, A. Bois, S. LaRochelle and W. Shi are with the Department of Electrical and Computer Engineering, Centre d'Optique, Photonique et Laser (COPL), Université Laval, Québec, Québec, Canada (e-mail: raphael.dube-demers.1@ulaval.ca; wei.shi@gel.ulaval.ca).

Q. Zhong and D. V. Plant are with the Department of Electrical and Computer Engineering, McGill University, Montréal, Québec, Canada.

M. Caverley, Y. Wang and L. Chrostowski are with the Department of Electrical and Computer Engineering, University of British Columbia, Vancouver, British-Columbia, Canada.

principle, numerical tools can be used, but analytical means are critical. They play a pivotal role in our understanding and, when guardedly implemented, are efficient and reliable.

Most of the available characterizations are built out from static transfer functions and inherently fail to predict many important features. Hitherto, frequency response has often been estimated by the RC constant and photon lifetime [1]. Time-domain descriptions are traditionally based on the coupled-mode theory (CMT) [3], however this approach is not precise for cavities with low finesse. More recently, derivations for small-signal operations have been presented [4] but don't accurately predict large-signal operations. In addition, the modulator response can be modeled via proprietary software. For example, the ring can be represented by a discrete set of sub-components where the dynamical response is computed through the photon propagation across the resonator for multiple round-trips [6]. By extension of the circuit model in [6], the analytical expressions presented here model the dynamical response of the resonator, i.e. our equations represent the time-dependent response of the circuit model.

Another solution is based on the time-dependent solution of the transfer function for microring modulators [5]. However, this approach is incomplete when the time dependence is present over more than one parameter (phase, loss or coupling), as it is the case for intra-cavity modulation, for example. Furthermore, the electrical dynamics of the p-n junction has to be considered since it imposes limitations at high-frequency operation.

In this paper, we put forward and substantiate a comprehensive analytical model for microring and microdisk modulators. It is noteworthy that the model represents the analytical transformation of known physical inputs and parameters into time-dependent optical responses, consolidating the bridge between device designs and

system analysis. In particular, we show that the usual representation based on the quality factor is not sufficient to fully consider the effect of detuning on the modulation bandwidth. Also, unless specifically stated, the analytical means apply directly to both the microring and microdisk modulators.

The rest of this paper is organized as follows, sec. II describes the analytical model. Specifically, it provides the model we use to represent the electrical behavior of the p-n junction and the carrier distribution. We then present how we compute the optical mode profile and effective index. The free-carrier plasma dispersion effect is used to model the interaction between material and optical waves. Finally, this section contains details about novel time-dependent solutions of the transfer function for optical modulation. These solutions are the rigorous analytical solutions of the time-dependent transfer matrix formulation. They represent the particular case of intra-cavity modulation and the general case. Sec. III presents the application of the model along experimental data. It begins by the verification of static behaviors. It follows with the validation of the model for small and then large-signal regimes of operation. Sec. IV presents a discussion on some peculiarities of our model, i.e its accuracy and scalability. Also, we discuss the ability to predict large-signal, time-domain pulse shapes and consequently, the ability to investigate the chirp. Extra details are presented in the appendixes.

II. ANALYTIC MODEL

Fig. 1 explains in a visual manner how the model is structured. We first consider the electrical dynamics of the p-n junction since the effective optical modulation results from the electrical potential that exists at the boundaries of the p-n junction. To that extent, we consider the carrier distributions as a function of the applied voltage. This first step is represented by block A. The second step, represented by block B, is to model the optical electromagnetic field inside the waveguide. The overlap between the carrier distributions and optical mode is computed to obtain the change in effective index, and is represented by block C. The last step, represented by block D, uses changes in physical parameters to compute the time-dependent transfer matrix solution of the microring/microdisk resonators.

We assume each section to be independent of each other, we thereupon avoid creating one complex and cumbersome monolithic block. Instead, the effort is split between different, smaller building blocks. It is a crucial step if one wants to gain in understanding and computational efficiency. Moreover, doing so makes the model highly customizable and scalable. As an example, the modeling of a more complicated p-n junction, e.g. a wrap-around p-n junction [7], would require changes in
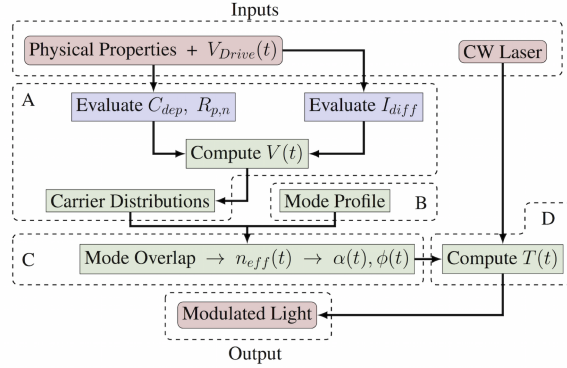

Fig. 1. Schematic representation of the model. From the ideal driving voltage and physical parameters, we evaluate the contribution of diffusion and depletion mechanisms. It is then possible to compute the voltage at the boundaries of the space-charge region and consequently, the carrier distributions (Sec. II-A). The mode profile is obtained from the waveguide geometry (Sec. II-B). The effective index as a function of voltage is computed by the overlap between the mode profile and the carrier distributions (Sec. II-C). The final step is to compute the corresponding time-dependent transfer coefficient (Sec. II-D). The novel equations presented in the latter subsection represent the core of our model.

block A and B, whereas the remaining framework retains its applicability.

A. Electrical dynamics of the p-n junction

We consider a lateral p-n junction configuration that is widely used in silicon modulators with CMOS compatible photonic process [8]. Fig. 2 shows a schematic of the microring p-n junction. In this work, forward bias is denoted by a positive voltage and reverse bias by a negative voltage.

The knowledge of the electrical behavior of the p-n diode is vital to determine the modulation response. Since the contributions of the diffusion and depletion mechanisms change significantly as a function of the applied electrical bias, the investigation of each regime is necessary. Thus we distinguish between three situations, that is the applied electrical potential can either be positive, negative or absent.

1) Equilibrium: In the absence of external electrical potential, we can approximate the built-in potential V_{bi} that exists between the boundaries of the depletion region by assuming that the product of the free-charge densities is independent of the Fermi energy, i.e. $d\left(p_0 n_0\right)/dt = 0$ where $p_0(n_0)$ is the excess minority holes(electrons) densities. Hence, solving the Poisson's equation while implementing the Einstein-Smoluchowski relation and the aforementioned approximation allows the calculation of the built-in potential V_{bi} [9]

$$V_{bi} = \frac{k_B T}{2q} \ln\left(\frac{N_A N_D}{p_0 n_0}\right) \tag{1}$$
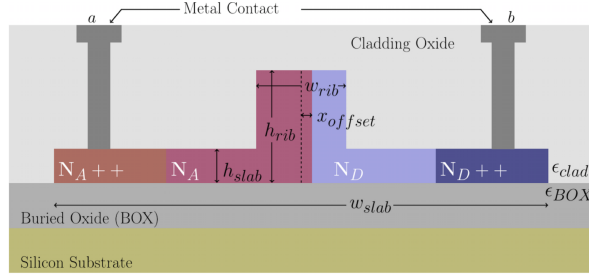
(a)

(b)

Fig. 2. Cross-sectional view of the p-n junction in a ridge waveguide. a) Implantation profile and physical dimensions of the waveguide. b) 1-D free-carrier distributions, (not at scale) with carrier profile, depletion region and dimensions.

where k_B is the Boltzmann constant, T is the temperature, q is the elementary charge and N_A and N_D are respectively the acceptors (P region) and donors (N region) densities. As can be seen in Fig. 2, and throughout this paper, we assume that the p-n junction is represented by an abrupt junction where the dopant profiles are represented by step changes at the dopant boundaries, i.e. a shallow-diffused junction. We shall also assume the p-n junction to be in the short-base limit, i.e. the diffusion length is comparable to the junction length [10]. The last approximation yields a quasi-linear distribution of the excess minority carrier densities between the depletion region and the heavily doped regions. We assume that the presence of the P_{++} and N_{++} regions does not affect the shape of the depletion region, therefore, they can be treated as simple ohmic resistances.

2) Forward bias: It is important to underline that we do not explicitly implement the forward bias regime in this paper. One of the reasons is that, for the usual dopant densities used in silicon-on-insulator (SOI), the minority carrier lifetimes are roughly around $10^{-6}-10^{-7}$ seconds for bulk silicon [11], [12] and around 10^{-9} seconds for patterned silicon [13], [14], which is not ideal for high-speed operation. In addition, one regime of operation, reverse bias for instance, is sufficient to demonstrate the capability of our approach.

In spite of this choice, it is noteworthy that forward bias regime of operation can be implemented via the so-
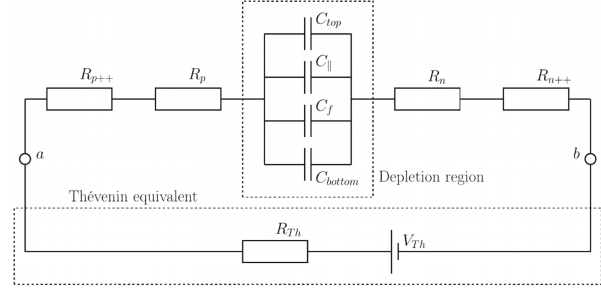

Fig. 3. Circuit model for the reverse biased (depletion mechanism) p-n junction. The external circuit is encompassed by the arbitrary Thévenin equivalent.

called *charge-control* model [15]. Yet, this model fails to predict the frequency dependence of the diffusion current. Nonetheless, analytical expressions that correctly represent that dependence are readily available [16].

3) Reverse bias: The current from the diffusion mechanism and the one that arises from a voltage variation (depletion capacitance) are additive [16], [10]. For the reverse bias mode of operation, as the voltage goes from 0 to negative values, the depletion region becomes wider and the depletion capacitance decreases. The presence of the depletion region also means that the diffusion current is negligible as soon as $|V| \gg q/k_B T$, where V is the applied voltage. Therefrom, it is reasonable to assume that the electrical dynamics of the p-n diode is dependent only on the depletion mechanism.

In this paper, we implement the RC model that can be found in [17], which has the advantage of being all analytical. In this model, the electrical dynamic of the P and N regions is encompassed by the depletion capacitances (C_{top}, $C_{\parallel}$, C_f, C_{bottom}) and resistances (R_p, R_n), as shown in Fig. 3. Details about the computation of the aforementioned depletion capacitances and resistances are presented in App. I. We add the resistances (tabulated sheet resistances) of the P_{++} and N_{++} regions. The circuit is completed by the external circuit which is represented by a Thévenin equivalent, here a voltage source V_{Th} in series with a resistance R_{Th}.

The correspondence between the ideal source V_{Th} and V being linear, such a RC circuit is easily studied by means of Laplace transform. Finally, note that the inclusion of both mechanism (diffusion and depletion) leads to a model that can predict turn-on and switching transients.

4) Free-carrier distributions: The free-carrier distributions are needed in order to compute the change in effective index. With respect to our model, we consider that the carrier distributions follow the potential V at the boundary of the diode. We therefore consider the time-dependence as included in the RC model. Thus, under the quasi-neutrality approximation, we assume that

4

the distributions are represented by their steady-state solutions [10], hence hole/electron distributions are

$$\{p, n\} = \{p_0, n_0\} \left(e^{\frac{qV}{k_B T}} - 1 \right) \times$$
$$\left[\cosh\left(\frac{x}{L_{p,n}} - \coth\left(\frac{w_{D(n,p)}}{L_{p,n}} \right) \sinh\left(\frac{x}{L_{p,n}} \right) \right) \right] \quad (2)$$

where $L_{p,n}$ is the hole/electron diffusion length and x represents the distance from the physical separation in the middle of the junction (dopant boundary). The equilibrium carrier densities are given by

$$p_0 = \frac{n_i^2}{N_D} \quad , \quad n_0 = \frac{n_i^2}{N_A} \quad (3)$$

where n_i is the intrinsic carrier density. As discussed above, for the short-base limit, it is possible to simplify the carrier distributions (2) by noting that $\cosh(x/L_{p,n}) \sim 1$ and $\sinh(x/L_{p,n}) \sim x/L_{p,n}$. Such an approach linearizes the carrier distributions [18].

B. Optical mode profile

We use the effective index method [18], [19] to compute the 1-D mode profile. The use of such an approximation is reasonable because the errors in the mode profile are mainly at the corners of the waveguide in comparison to rigorous 2-D mode profiles [18]. As we will see in the next subsection, optical modulation is determined by the overlap between the mode profile and varied carrier distributions in the depletion region inside the waveguide core. Hence, the contribution of the mode profile error to the error in the change of effective index is negligible. Further discussions with simulation will be given in the next section.

However, the traditional effective index method cannot be directly applied to microdisks. The workaround is to introduce the angular dependence of the mode by solving a 2-D problem. This approach takes into account the bending of the waveguide, which is absent from the traditional effective index method. The diffusion formalism, as presented in [20], is a convenient way to obtain the new transcendental equation that describes the propagation. It is also important to underline that this method can also be used for a microring when one wants to take into account the bending of the ring. Ultimately, the diffusion formalism can be used for arbitrary resonator shapes as an extension of the present model.

For a 2-D circular dielectric of radius r, the characteristic equation is [21]

$$\eta_{12} \mathcal{H}_m (n_1 kr) \frac{d\mathcal{J}_m (n_1 kr)}{dk} =$$
$$\mathcal{J}_m (n_1 kr) \frac{d\mathcal{H}_m (n_2 kr)}{dk} \quad (4)$$

where $\mathcal{J}_m$ and $\mathcal{H}_m$ are the first kind Bessel and the first kind Hankel functions, respectively; n_1 and n_2 are the effective indexes of the inner and outer dielectrics, as computed through the 1-D effective index method; η_{12} is a polarization dependent factor, which is n_2/n_1 for the TE polarization and n_1/n_2 for the TM polarization.

The solutions (k) of (4) are the eigen-wavenumbers of the resonators. For each angular order m there is a set of eigenvalues defined by their radial order j. The whole sets of $k_{m,j}$ determine the skeleton of any excitation. So, at a resonant frequency, the mode that will be the most significant will be the least leaky one, i.e. the fundamental mode. Now, using the fact that, on resonance, the fundamental mode must be a solution of $m = n_{\text{eff}} kr$, one can compute the effective index.

Then we use the infinite angular degeneracy of the modes to solve for the radial field distribution. The solution that satisfies the cylindrical Helmholtz equation and represents the radial mode profile ψ inside the disk is

$$\psi(\rho) \propto \mathcal{J}_m (n_{\text{eff}} k_0 \rho) \quad (5)$$

where ρ represents the distance from the center of the disk. It is important to note that (5) is valid for both TE and TM polarization. Mode profiles are polarization dependent through the effective index.

C. Interaction between material and optical waves

We take the following steps in order to translate the inputs, such as the physical geometry and applied voltage, into useful outputs, such as the changes in phase and optical absorption. We first compute the change in refractive index due to the presence of free carriers introduced by doping the silicon. We then use the method described above to obtain the effective refractive index and mode profile. The third step is to compute the free-carrier distributions. The knowledge of both mode profiles and charge carrier distributions allows the computation of the overlap between them, hence the voltage-dependent change in effective index, loss, and phase. The last step gives us necessary parameters to proceed to our time-dependent solutions that will be given in the next subsection. An analogous approach has been taken in a frequency domain analysis [18].

1) Plasma dispersion effect: The presence of free carriers in silicon allows optical modulation, as predicted by Soref and Bennett in 1987 [22]. It is often convenient to describe the plasma dispersion effect over a wide range of wavelengths. Using the Drude model [18], [23], the change of refractive index Δn_{Si} and the excess loss $\Delta\alpha_{Si}$ due to the free-carrier absorption are given by

$$\Delta n_{Si} = -3.64 \times 10^{-10} \lambda_0^2 \Delta n - 3.51 \times 10^{-6} \lambda_0^2 \Delta p^{0.8} \quad (6a)$$
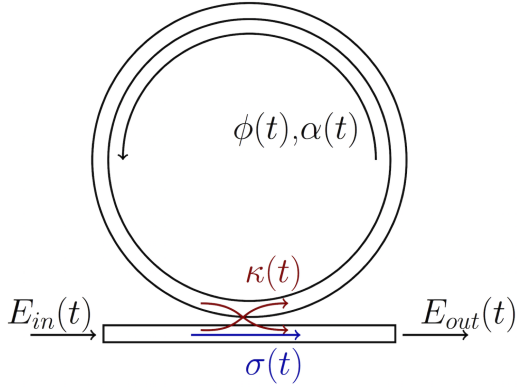
Fig. 4. Schematic of a microring modulator.

$$\Delta\alpha_{Si} = 3.52 \times 10^{-6}\lambda_0^2\Delta n + 2.4 \times 10^{-6}\lambda_0^2\Delta p \quad . \tag{6b}$$

Note that the coefficients given above assume that the wavelength is given in meter and the carrier per cubic centimeter. The change in absorption is in per centimeter.

2) Change in effective index: The change in effective index is computed by the overlap between the optical electric field and the charge-carrier distributions. The effective index $n_{\text{eff}}(V)$ that depends on the electrical potential is given by [18]

$$n_{\text{eff}}(V) = n_{\text{eff}} + \frac{dn_{\text{eff}}}{dn_{\text{Si}}} \times \\ \frac{\int E^*(x)\Delta n_{\text{Si}}(x,V)E(x)dx}{\int E^*(x)E(x)dx} \quad . \tag{7}$$

Here $dn_{\text{eff}}/dn_{\text{Si}}$ represents the variation of the modal effective index n_{eff} with respect to the variation in silicon refractive index n_{Si}. This value is usually quite close to 1. The knowledge of the electric field $E(x)$ and his complex conjugate $E^*(x)$ comes from the mode profile solved as described above. The phase modulation $\Delta\phi$ is computed from (7)

$$\Delta\phi = \frac{2\pi\Delta n_{\text{eff}}}{\lambda_0} \quad . \tag{8}$$

Intra-cavity modulation means that there is also a loss modulation. By the same justifications, the attenuation $\alpha(V)$ is

$$\alpha(V) = \frac{\int E^*(x)\Delta\alpha_{\text{Si}}(x,V)E(x)dx}{\int E^*(x)E(x)dx} \quad . \tag{9}$$

The voltage dependent effective index and loss given by (8) – (9) can be translated into time-dependent parameters as functions of time-dependent voltage $V(t)$, which will be used in the dynamic model to be presented below for optical modulation.

D. Time-dependent solutions for optical modulation

The response of a microring or microdisk resonator is determined by the phase shift $\phi(t)$ and the propagation loss $\alpha(t)$, as well as the straight-through and cross-over coupling coefficients, $\sigma(t)$ and $\kappa(t)$. A schematic representation of a microring resonator with an all-pass configuration is given in Fig. 4, where the transmission coefficient T is defined by $E_{out} = TE_{in}$.

The static transfer function of the transmission coefficient, T_s, is given by [24]

$$T_s = \frac{\sigma - \Lambda e^{-i\Phi}}{1 - \Lambda\sigma e^{-i\Phi}} \tag{10}$$

where Λ and Φ represent the round-trip attenuation and phase shift, respectively. Yet, (10) represents a particular case of a more complicated system. As a matter of fact, the dynamic transfer coefficient T_d is represented by a Fredholm integral equation of the second kind [5]

$$T_d(t) = \sigma(t) - \frac{\kappa(t)}{\kappa(t-\tau)}\Lambda(t)e^{-i\Phi(t)} + \\ \int_{-\infty}^{\infty} \frac{\kappa(\xi+\tau)}{\kappa(\xi)}\Lambda(\xi+\tau)\sigma(\xi)e^{-i\Phi(\xi+\tau)} \times \\ \delta(\xi - (t-\tau))T_d(\xi)d\xi \tag{11}$$

in which τ is the photon round-trip time across the ring. It is interesting to note that, in general, Fredholm (or sub-type Volterra) equations arise in the description of systems that have an *hereditary*, or *fading memory* [25]. The memory effect here described is the conceptual analog of the photon lifetime inside the cavity, in the sense that they both describe the dynamical storage of light inside the resonator.

To achieve optical modulation, at least one parameter in (11) must be time-dependent. A particular case, where only one parameter in (11) is time-dependent, has been addressed [5]. Here, we provide a general solution for simultaneous modulations of loss, phase, and coupling:

$$T_d(t) = \sigma(t) - \frac{\kappa(t)}{\kappa(t-\tau)}\Lambda(t)e^{-i\Phi(t)} + \\ \kappa(t)\sum_{n=1}^{\infty}\frac{1}{\kappa(t-n\tau)} \times \\ \left[\sigma(t-n\tau) - \frac{\kappa(t-n\tau)}{\kappa(t-(n+1)\tau)}\Lambda(t-n\tau)e^{-i\Phi(t-n\tau)}\right] \times \\ \prod_{m=0}^{n-1}\Lambda(t-m\tau)\sigma(t-(m+1)\tau)e^{-i\Phi(t-m\tau)} \quad . \tag{12}$$

Details on how we solve the Fredholm integral equation (11) are provided in App. II.

For intra-cavity modulation, only $\Phi(t)$ and $\Lambda(t)$ are functions of time. This approximation is justified by the fact that the p-n junction does not overlap with the
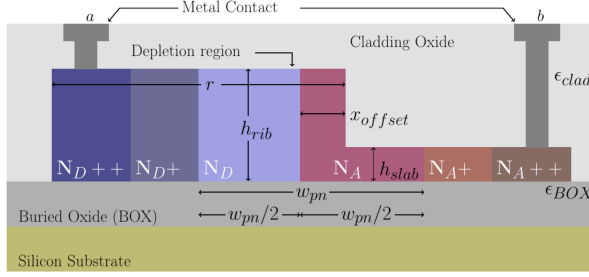
Fig. 5. Cross-sectional view of the p-n junction in the microdisk modulator.

Table I
PHYSICAL PARAMETERS OF THE FABRICATED DEVICES.

Microring

r	$10\ \mu m$	diode span L	$0.75 \cdot 2\pi r$
w_{rib}	$0.5\ \mu m$	h_{rib}	$200\ nm$
h_{slab}	$90\ nm$	x_{offset}	$120\ nm$
T	$294.15\ K$	n_i	$1e10\ /cm^3$
N_A	$8e17\ /cm^3$	N_{A++}	$4.4e20\ /cm^3$
N_D	$2.4e18\ /cm^3$	N_{D++}	$4.4e20\ /cm^3$
w_{pn}	$1.2\ \mu m$	coupler gap	$190\ nm$
μ_e	$364\ cm^2/(Vs)$	$R_s\ (N_{++})$	$45\ \Omega$
μ_h	$205\ cm^2/(Vs)$	$R_s\ (P_{++})$	$59\ \Omega$
$\mathcal{F}_{N++}$	0.14	$\mathcal{F}_{P++}$	0.14

Microdisk

h_{slab}	$90\ nm$	h_{rib}	$220\ nm$
N_A	$5e17\ /cm^3$	N_D	$3e17\ /cm^3$
N_{A+}	$2e18\ /cm^3$	N_{D+}	$2e18\ /cm^3$
N_{A++}	$4.4e20\ /cm^3$	N_{D++}	$4.4e20\ /cm^3$
μ_e	$422\ cm^2/(Vs)$	μ_h	$416\ cm^2/(Vs)$
r	$10\ \mu m$	coupler gap	$200\ nm$
w_{pn}	$1.1\ \mu m$	x_{offset}	$350\ nm$
$\mathcal{F}_{N++}$	$6.8e-2$	$\mathcal{F}_{P++}$	$2.5e-2$
$\mathcal{F}_{N+}$	$1.1e-2$	$R_s\ (N_+)$	$1610\ \Omega$
$\mathcal{F}_{P+}$	$9.1e-3$	$R_s\ (P_+)$	$2820\ \Omega$

coupling region in the particular devices under study. We also assume a loss-less coupler. Thus, the expression for the transfer function becomes simpler

$$T_d(t) = \sigma - \Lambda(t)e^{-i\Phi(t)} +$$
$$\sum_{n=1}^{\infty} \sigma^n \left[\sigma - \Lambda(t - n\tau)e^{-i\Phi(t-n\tau)} \right] \times$$
$$\prod_{m=0}^{n-1} \Lambda(t - m\tau) e^{-i\Phi(t-m\tau)} \ . \tag{13}$$

Note that the intrinsic hereditary memory effect in (11) is carried by both the solutions given by (12) and (13).

III. SIMULATION AND EXPERIMENTAL VALIDATION

This section presents the application of the aforementioned model along experimental data. For the demonstration purpose, we consider a microring modulator and a microdisk modulator that were fabricated by IME, Singapore. The parameters of the fabricated devices are given in Table I. Most parameters of the microring modulator are labeled in Fig. 2. Definitions of other parameters include sheet resistance R_s and form factor $\mathcal{F}$ (length/width) of the N_{++} and P_{++} slab regions. Taking the product of the sheet resistances and the form factors yields the ohmic resistances of these regions.

The waveguide cross-section of the microdisk modulator, applying three levels of dopants on each side of the diode, is shown in Fig. 5. In this case, x_offset denotes the distance from the edge of the disk to the center of the p-n junction. The P and N regions are symmetrical with respect to x_offset. The width of the lightly doped region is given by w_{pn}, as for the microring.

The coupling coefficients are calculated using rigorous 3-D FDTD simulations [37], which give $\kappa = 0.29$ and $\kappa = 0.28$ for the microring and microdisk, respectively.

In the rest of this section, we examine the performance of the modulators and compare simulation with experiment. We first look at the static response, providing the computed mode profiles, changes in effective index, and absorption and transmission spectra. Then we examine the small-signal behavior. Finally, we consider large-signal modulation.

A. DC performance

The measured power transmission spectrum for different DC bias is presented in Fig. 6. The first thing to notice is the overall tendency, showing that the ring is under-coupled, i.e. $\Lambda < \sigma$. Recall that we distinguish between two main regimes of operation for the p-n diode, that is forward and reverse bias, the former regime being dominated by the diffusion current and the latter being dominated by the depletion mechanism. As the reverse bias increases, (18) tells us that the depletion
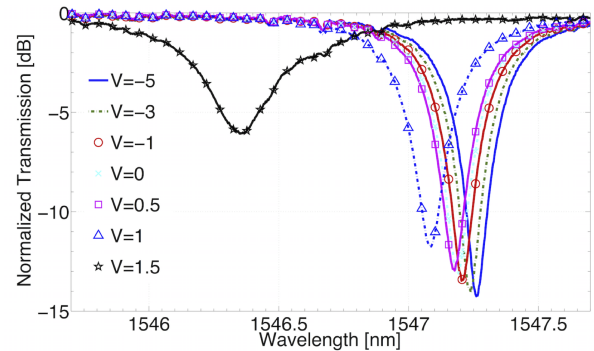

Fig. 6. Measured power transmission spectrum of the microring modulator for various electrical excitations. The DC voltage is noted in unit of Volt.
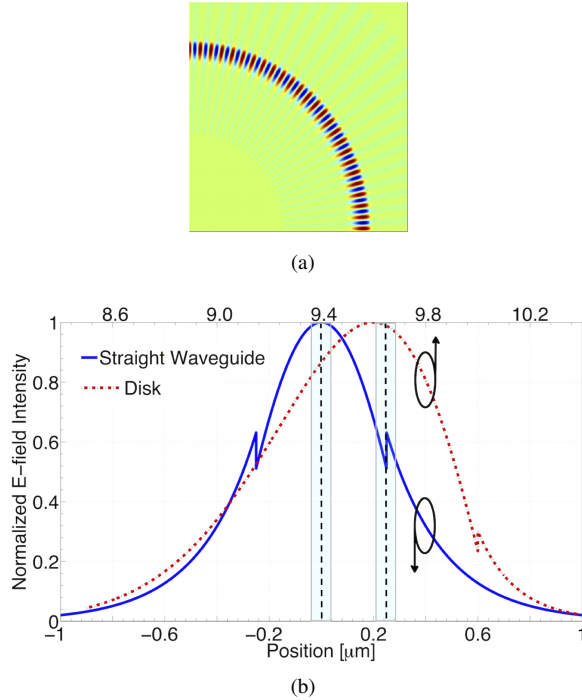
(a)

(b)

Fig. 7. a) Reconstructed 2-D mode profile for the $R = 10\ \mu m$ microdisk, $m = 101, j = 1$ at $\lambda = 1547.13$ nm. b) 1-D mode profiles for the straight waveguide and disk, again at $\lambda = 1574.13$ nm. The top axis shows the position, in μm, from the center of the disk and the bottom axis shows the position relative to the center of the straight waveguide. The light blue rectangles show the position and size of the depletion regions with the dotted vertical lines denoting the center of the depletion regions.

region becomes wider, indicating a smaller mode overlap with free carriers and thus lower optical attenuation. Therefore, Λ becomes closer to σ as the reverse voltage increases, approaching to the critical coupling condition, for a higher extinction ratio.

Now, considering the case where V increases above 0, we see that the coupling is far from critical, indicating significant attenuation. Actually, near zero bias (e.g., $V = 0.5$ V) the center wavelength shift and change in excitation ratio are comparable to those under reverse bias, as shown in Fig. 6. This suggests a very low forward current, which is what we expect as (1) predicts $V_{bi} \simeq 0.95$ V. As expected, the curve at $V = 1$ V shows a significant deviation due to a significant current. This deviation is even greater for the case $V = 1.5$ V, showing an exponential like behavior, a typical characteristic of diode I-V curves. These observations have verified that we can neglect the diffusion current when operating in reverse bias condition, whereas we cannot neglect it when operating in forward bias condition.

Fig. 7 shows calculated mode profiles of the microring and microdisk. The comparison of the 1-D profiles makes clear that, the effective index method does not
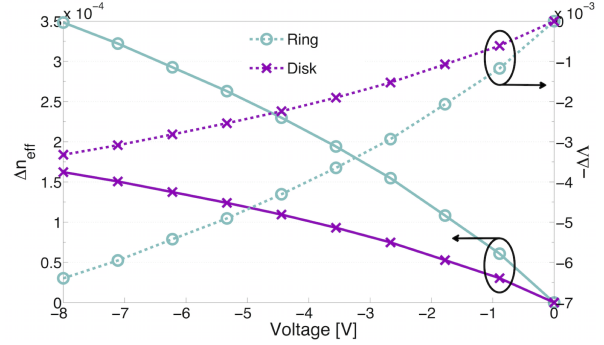

Fig. 8. Change in effective index (n_{eff}, left) and attenuation (Λ, right) with respect to equilibrium, i.e. $V = 0$ V.

take into account the bending of the waveguide for the microring, whereas it does for the microdisk. However, as discussed in [27] for the microring, the bending contribution to the loss is negligible at a bending radius of 10 μm. This suggests that the mode profile is relatively unchanged. We further compute the mode overlap between a straight waveguide and a bent one, which is is as large as 99.9% for $r = 10\ \mu m$.

Fig. 8 shows the calculated changes in effective index and attenuation as functions of applied voltage, using (7), (9). The microring shows higher changes in both effective index and optical attenuation. This is because of the fundamental difference between the mode profiles of the microring and microdisk. The mode of the microdisk is not constrained in the inner side, making it strongly asymmetrical and broader. Thus, the microring has a better overlap between the optical field and the depletion region and thus higher modulation efficiency.

We now present experimental verification of our model starting with its static response. As described in the previous section, our model allows the computation of all the parameters needed as inputs to the equations that describe the transmission. Once these parameters are calculated, we can compute the microring transmission using (12). Fig. 10 shows the simulated and measured transmission spectra of the microring modulator with varied DC bias.
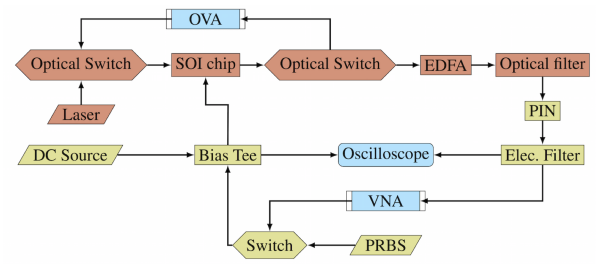

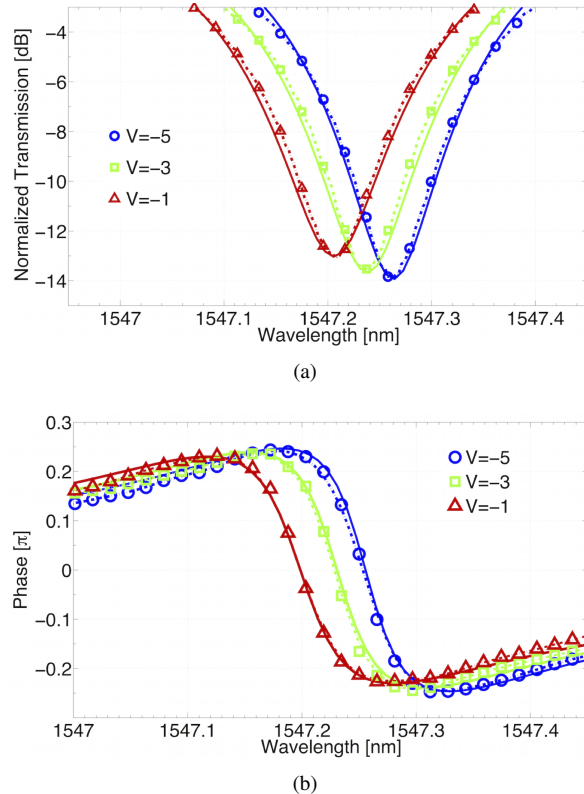Fig. 9. Block diagram that represents our test bench.

(a)

(b)

Fig. 10. a), b) Measured (dashed lines) and computed (solid lines) power transmission coefficients and phase profiles, respectively. Note that the extinction ratio is increasing with the magnitude of V, which is a signature of under coupling conditions. The phase profile also shows under coupling, i.e. the total phase shift is less than π. Also, we measured the group delay and extracted the phase response via numerical integration of the group delay.

The phase response is extracted from the group delay measured using an optical vector analyzer (Luna). A block diagram that illustrates our experimental setup is shown in Fig. 9. In Fig. 10, we observe an excellent agreement between simulation and experiment, thus confirming the validity of the approach.

B. Small-signal responses

In order to compute the dynamic response, we start by computing the cut-off frequency of the electrical circuit (Fig. 3), as presented at Fig. 11. We use the usual definition for the cut-off frequency, i.e. $f_{ele} = (2\pi RC)^{-1}$, where R and C are the total resistance and capacitance of the electrical circuit. It is easy to see that the capacitance decreases as the magnitude of the voltage increases, yielding a higher bandwidth. However, a closer look shows that the slope becomes lower as the magnitude of the voltage increases, indicating a lower change in the width of the depletion region. Accordingly, there exists a trade-off between the modulation speed and the modulation amplitude. The complete picture is more complicated since the modulation amplitude is also a function of the coupling condition of the resonator.

Now we include the optical contribution to the total bandwidth of the device. The frequency response (S_{21}) of the microdisk modulator, measured using a vector network analyzer, is shown in Fig. 12. The figure presents two measurements, both done at a bias of -3 V but with varied frequency detuning from the resonance wavelength. This bias is chosen arbitrarily for illustration. Similar results are obtained between -6 V to 0 V. Along the measurements come the computed results. We obtain excellent agreement for up to 36 GHz, after that, the signal becomes noisy as it approaches the noise floor. In order to calculate S_{21}, we first simulate time-domain response of the RC circuit using a square-shaped 10 mV pulse of 1 ps. Then, the optical response is computed using the electrical response. The frequency response is finally obtained by taking the discrete Fourier transform (DFT) of the optical response in the time domain. Hence, the cut-off frequencies are readily available from the DFT results.

It is noteworthy that the computation is able to correctly predict the *modulation resonance*. Such a resonance can be easily seen for a detuning frequency of 10 GHz. It is here demonstrated that the 3-dB bandwidth strongly depends on the detuning frequency. This is another motivation for such a model since the usual representation of the cut-off frequency, which is based on the photon lifetime, e.g. the one described in [28], cannot represent this particular behavior.

Computing the S_{21} with and without the inclusion of the p-n junction allows one to determine its contribution to the total bandwidth. To that extent, we showed in a previous work [29] with the microring described in Table I, that the contribution of the p-n junction to the total bandwidth is significant and cannot be neglected. In fact, for this particular case, the sole optical model yields a bandwidth around 43.1 GHz, whereas the combined model yields a bandwidth of 32.5 GHz.
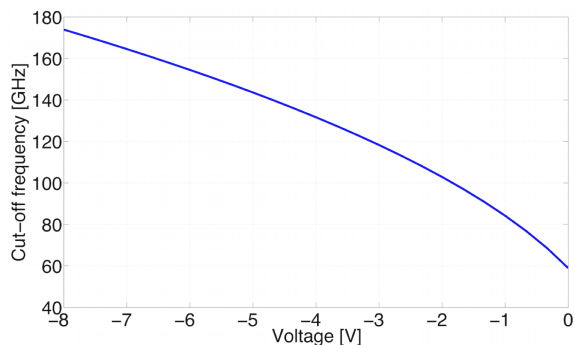

Fig. 11. Computed cut-off frequency for the microring's p-n junction. We assumed a Thévenin resistance of 50 Ω.
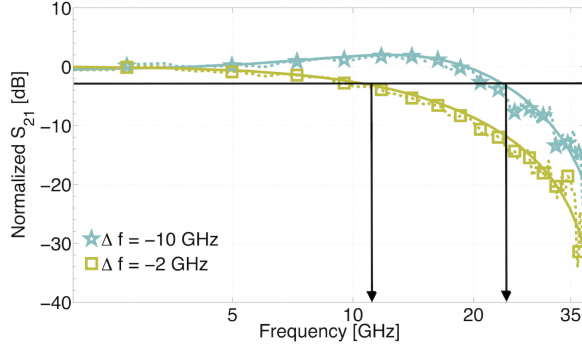
Fig. 12. Measured and computed scattering parameter S_{21} for the microdisk. The two curves are done at a bias of -3 V, one with a detuning of -10 GHz and the other with a detuning of -2 GHz from the resonant frequency. We observe the 3-dB cut-off frequency to be 23.8 GHz and 10.6 GHz for a detuning of -10 GHz and -2 GHz, respectively. All results are normalized at $f = 1$ GHz.

With the results presented in Table I, [29] and Fig. 11, we can now verify whether the usual description based on the quality factor is accurate [1]. Interestingly, the device bandwidth estimated by

$$\frac{1}{f_T^2} = \frac{1}{f_{opt}^2} + \frac{1}{f_{ele}^2} \tag{14}$$

is inaccurate; where the terms represent the total, optical and electrical bandwidth, respectively. Here, we have considered that the electrical bandwidth is roughly 100 GHz at -2 V of bias, as seen in Fig. 11. With an optical bandwidth computed at 43.1 GHz, the predicted total bandwidth is 39.6 GHz instead of the observed 32.5 GHz. In fact, the optical bandwidth is usually defined as

$$f_{opt} = \frac{\omega_0}{2\pi Q_T} \tag{15}$$

where ω_0 is the optical frequency and Q_T is the total quality factor that is given by [37], [18]

$$Q_T = \left[\frac{\lambda_0 \ln|\sigma|}{2\pi^2 r n_g} + \frac{\lambda_0 \alpha}{2\pi n_g} \right]^{-1} \tag{16}$$

where n_g is the group index. However, (16) does not carry phase information and hence does not distinguish between detuning states [30]. In contrast, in the model that we propose, the presence of the phase term Φ in (11) allows the latter to distinguish between detuning states. The complete time-dependent description (11) therefore represents the detuning and allows reliable bandwidth predication compared to the estimate provided by the quality factor.

C. Large-signal responses

The prediction of large-signal modulation is readily available by our modeling approach. As a proof of
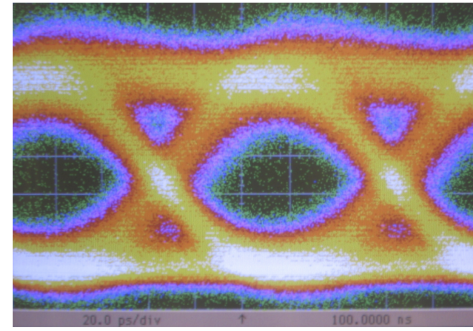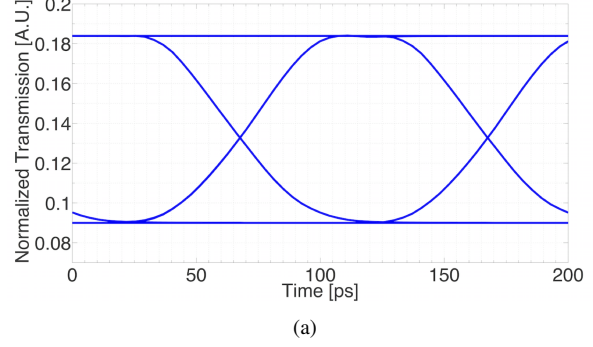

(a)

(b)

Fig. 13. a) Theoretical prediction of the eye diagram for a detuning of 5.6 GHz, biased at -3 V. The driving voltage is $V_{pp} = 3.5$ V at a frequency of $f = 10$ Gbit/s with a 2^{15} PRBS pattern. b) Corresponding experimental eye diagram for a OOK, NRZ modulation scheme after roughly 5 minutes of data acquisitions (infinte persistance).

concept, we measure the eye diagram of a microring modulator. The microring under study is slightly different from the one described in Table I. The only differences are that the level of dopants in the N_A and N_D regions are the same as the microdisk. Moreover, the width of the central p-n junction is much more wider, i.e. $w_{pn} = 2$ μm. Also, the p-n junction is centered, i.e. $x_{offset} = 0$. These differences mean, in part, that the p-n junction is much more resistive, hence a lower bandwidth. This particular p-n junction also means that the optical losses inside the ring are much lower, hence, the optimal coupling is obtained with a greater coupler gap, here the physical coupler gap is 300 nm.

We obtain excellent agreement between the theory and experiment, Fig. 13. The predicted rise-time and fall-time for a $0\% - 100\%$ scheme are 80 ps and 82 ps, respectively, in a good agreement with the experimental results that are consistently measured around 82 to 84 ps. The slight mismatch may come from electrical parasitic from on-chip and off-chip electrical connections.

In the light of the above discussion, the capacity to predict in a reliable manner the large-signal operation allows one to study many interesting features towards system applications.
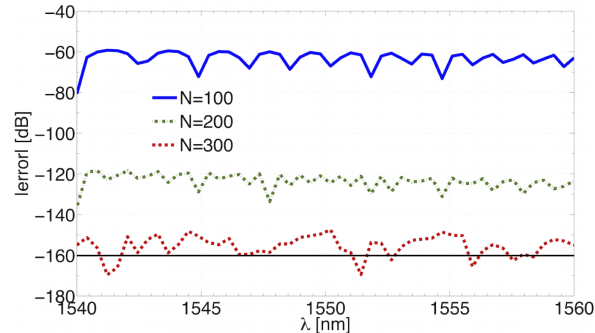
Fig. 14. Computed absolute error between the static (10) and dynamic (12) representations for different number of terms N kept in the serie. The computation is done using the microring parameters. The machine ϵ for double precision in decimal is shown by the black horizontal line.

IV. DISCUSSIONS

So far, the model has been explained and verified though the comparison with experiment. In this section, we discuss the accuracy of the model, in particular, the effective index method and the truncation error in the solution of the dynamic transfer function. We then discuss about the pulse shapes extracted from the model. Finally, we consider the scalability of our modeling technique.

A. Accuracy

We now consider how well the effective index method predicts a correct mode profile. For the microring, that question is answered in [18] that gives a good validation by comparing the effective index method mode profile with a rigorous FDTD solution, showing that the error committed on the effective index is around 1%. We do the same computation for the microdisk and we obtain an error around 2.5% for the effective index. Besides, we observe up to 7% of error, in a point-by-point comparison, over the mode profile computed through the effective index method. Fortunately, the error is negligible around the peak of the mode, where the overlap integrals are computed. Such low errors confirm the reliability of the effective index method that can dramatically reduce the computational burden while keeping a good precision.

Now, one might wonder about the truncation error. In fact, this error is unavoidable since, despite the analytical nature of (12), (13), the solutions are in the form of infinite series. The error between (12), (13) and (10), for the static case, is at the machine ϵ, i.e. the unit round-off, in double decimal precision, for typically less than 250 terms in the summation. Hence, the added computational cost associated with (12), (13) is negligible. Fig. 14 presents the error committed on the amplitude of the transmitted signal in the case of static transmission. It
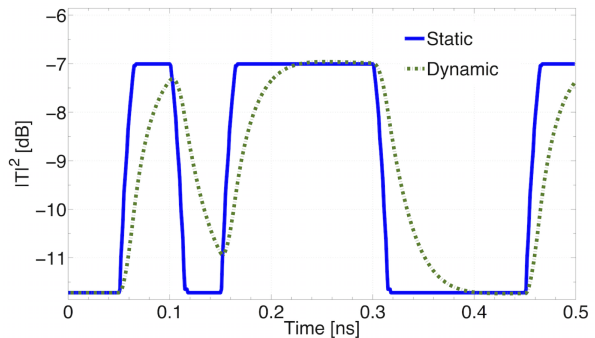
(a)
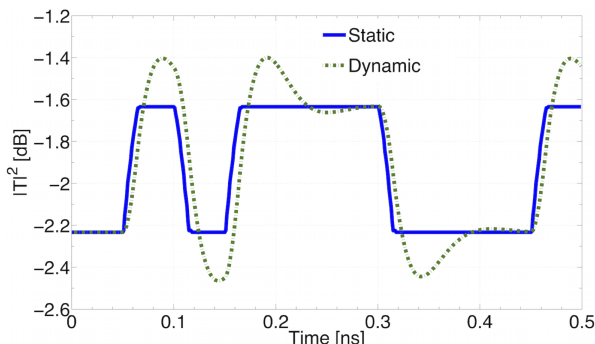
(b)

Fig. 15. a), b) Computed transmitted power for -2 GHz and -10 GHz detuning frequency, respectively. The solid lines show the results when (10) is used whereas the dashed lines show the results when (12) and (13) are used, i.e. both (12) and (13) lead to the same result since we consider intra-cavity modulation. Note that, for a steady excitation long enough, the static and dynamic model converge, as it is expected. $V_{p-p} = 2.5$ V as V is varied in the range -3 V to -5.5 V.

appears that the use of 300 terms ($N = 300$) is safe since the absolute error is at the machine ϵ. However, the error committed over n_{eff} is around -20 dB, therefrom, -60 dB of truncation error, i.e. $N \simeq 100$, is sufficient to retain good precision while being computationally negligible.

B. Pulse shapes

The availability of a large-signal model enables digital signal processing (DSP) and system level simulation. Without diving in the world of DSP, we want to underline some key features of our technique. Namely, the model produces reliable large-signal responses. In fact, the modulation resonance observed in small-signal analysis is also present in large-signal analysis, as can be seen in Fig. 15. This feature is of importance because it shows, for example, that the pulse shape is function of the detuning frequency, as it is the case for modulation amplitude. The resonator response versus detuning is analogous to the response of a classical, mechanical oscillator versus its damping state. That is, when the detuning is low, there is no overshoot, hence the analogue of a over-damped

oscillator and a high detuning corresponds to an under-damped oscillator, where there is an overshoot in the response.

The phase profile also behaves in a similar manner, that is, it exhibits under-damped and over-damped responses. Hence, phase and amplitude profiles must be taken together to complete the investigation of the modulation response. As an example, Fig. 16 presents the turn-on transient of the microring for -2 and -10 GHz of detuning, i.e. we consider a discrete transition from V=0 to V=-6 V. It is shown that both transients are chirped and that the chirp is a function of the detuning frequency. This extracted information supplements the need for a reliable large-signal model, e.g. the propagation of the pulses is a direct function of the chirp, which is, in turn, a direct function of the detuning and resonator's physical construction.

We can see the inherent complexity in choosing the optimal operation conditions: the optimal detuning and bias are not absolute and depend on a series of system-level considerations, e.g., the power budget, driving voltage, tolerance to chirped pulses, desired modulation depth, and etc.

C. Scalability

Last but not least, we discuss about the scalability of our model. As already shown, our model readily applies to various regimes, or, as suggested, can be used to analyze the chirping. Direct extensions of the aforementioned simulations include the systematic investigation of the power consumption and the inherent tradeoff between modulation bandwidth and efficiency. Besides, one particular application we foresee is pragmatic optimization of the modulator design. In fact, the analytical nature of the model means it can be implemented, via the definition of suitable cost functions, into the desired optimization routine. It is noteworthy that these cost functions can aim at different targets, i.e. from device optimization to system optimization.

Leveraging the block-like structure of the model, one can easily include and/or replace a block to include any desired physical contributions. Hence, the model is not restricted to the specific examples that have been presented. For example, the extension of this model to a Mach-Zehnder modulator (MZM) is straightforward as one only needs to replace the microring transfer function by the known MZM transfer function.

Finally, our model can be easily extended for more complex structures or systems such as cascaded microring modulators aimed at wavelength multiplexing, although complex structures may contain different modulator configurations.
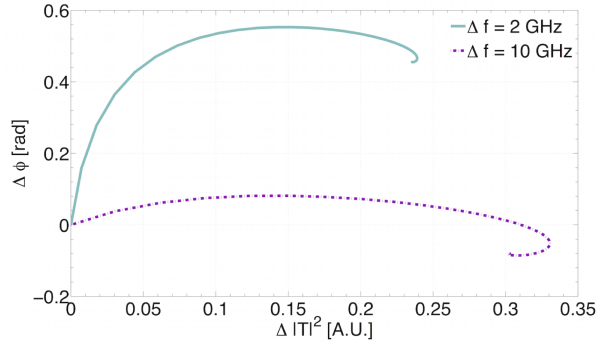

Fig. 16. Computed changes in phase as a function of amplitude for a turn-on from $V = 0$ V to $V = -6$ V. This computation is done with respect to microring parameters found in Table I at 2 different detunings.

V. CONCLUSIONS

We have proposed an analytical, comprehensive model for high-speed microring/microdisk modulators and verified its validity with a series of measurements where we obtained excellent agreement. In particular, we presented a general time-domain solution that carries the memory effect of the optical resonator. It is prominent that the model includes both optical and electrical dynamics.

The verification has been presented for both DC and AC operations where both small and large-signal regimes are investigated. Comparison with the traditional small-signal model, i.e. the quality factor based approach, has been made and showed that it does not represent the modulation resonance due to the detuning. Along the experimental validations, mode profiles, changes in effective index, absorption, carrier distributions and diode bandwidth are presented. It is noteworthy that we introduced a variation of the effective index method that takes into account the bending radius of the resonator. The contribution of the diode bandwidth is shown to be significant to the total bandwidth. Various inherent tradeoffs and possible applications are then discussed. Namely, the ability to compute the chirp of the modulated signal and the possibility to include other physical effects or dependencies. The truncation error is shown to be low for a reasonable amount of terms, demonstrating the high computational efficiency of the model.

In conclusion, the proposed analytical model is generally valid and complete. It is useful for design and optimization of microdisk/microring based modulators.

APPENDIX I
RC MODEL OF REVERSE BIASED P-N JUNCTIONS

The p-n junction under reverse bias is represented by a RC circuit model where the total capacitance is represented by 4 different contributions. The first contribution is the capacitance calculated assuming two
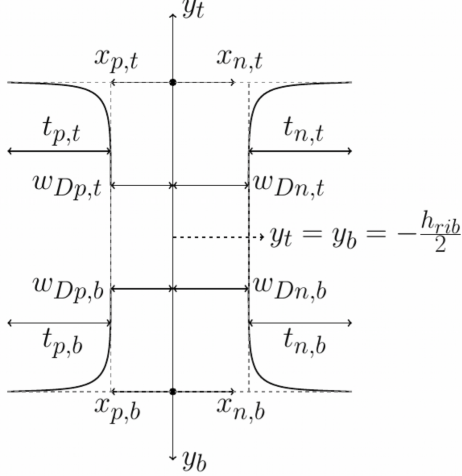
12

Fig. 17. Shape of the depletion region, not at scale. The parametric solutions are defined for two different sets of axis, one for the top half and the other for the bottom half, they match at $y_t = y_b = -\frac{h_{rib}}{2}$.

boundaries that are perfectly parallel and infinite, $C_\parallel$. The second contribution is the fringe capacitance C_f that comes from the fact that the parallel plates capacitor has finite dimension, here the extra bent field on the top and bottom edges. The last contribution arises in the form of co-planar strips (C_{top}, C_{bottom}) that takes into account the non-parallel interfaces of the free-charge distributions. The final depletion capacitance C_{dep} is given by the sum of each contributors, i.e. $C_{dep} = C_f + C_\parallel + C_{top} + C_{bottom}$. The parallel capacitance is simply

$$C_\parallel = \epsilon_0 \epsilon_S \frac{h_{rib}}{w_D} \qquad (17)$$

where ϵ_0, ϵ_S are respectively the free-space permittivity and the dielectric constant for silicon, and w_D is the width of the depletion region [31]

$$w_D = \sqrt{\frac{2\epsilon_0 \epsilon_S}{q} \left(\frac{N_A + N_D}{N_A N_D} \right) \left(V_{bi} - V - \frac{2k_B T}{q} \right)}. \qquad (18)$$

The fringe capacitance is given by [32], [33]

$$C_f = \epsilon_0 \left(\frac{\epsilon_{clad} + \epsilon_{BOX}}{2\pi} \right) \ln \left(2\pi \frac{h_{rib}}{w_D} \right) \qquad (19)$$

and the last contributions are given by [34]

$$C_{top,bottom} = \epsilon_0 \epsilon_{clad,BOX} \frac{\mathcal{K}(k')}{\mathcal{K}(k)} \qquad (20)$$

where $\epsilon_{clad,BOX}$ are the dielectric constant of the cladding and the buried oxide, and $\mathcal{K}(k)$ is the complete elliptic integral of the first kind [35]. The parameter k' is simply $k' = \sqrt{1 - k^2}$ where k is defined as $k = \sqrt{w_D (w_D + t_p)(w_D + t_n + t_p)/(w_D + t_n)}$. In the case where $\epsilon_{clad} \neq \epsilon_{BOX}$, one has to compute k

and k' as a function of $(t_{p,t}, t_{n,t})$ for the top part, i.e. use ϵ_{clad}, and $(t_{p,b}, t_{n,b})$ for the bottom part, i.e. use ϵ_{BOX}. Parameters t_p and t_n come from the parametric solution of the shape of the depletion region and denote the width of the co-planar strips for the P and N regions respectively, as shown in Fig. 17. The shape of the depletion region is parametrized in ϑ : $\vartheta \in [-\pi/2, 0]$ as

$$x_{p,(t,b)} = \frac{2w_{Dp,(t,b)}}{\pi} + w_{Dp} - \frac{4w_{Dp,(t,b)}}{\pi} \sin^2 \left(\frac{\vartheta}{2} \right) \qquad (21a)$$

$$x_{n,(t,b)} = \frac{4w_{Dn,(t,b)}}{\pi} \sin^2 \left(\frac{\vartheta}{2} \right) - \left(\frac{2w_{Dn,(t,b)}}{\pi} + w_{Dn} \right) \qquad (21b)$$

and

$$y_{t,b} = \frac{2w_{Dn,(t,b)}}{\pi} \left[\ln \left(\tan \left(\frac{\pi}{4} + \frac{\vartheta}{2} \right) \right) - \sin(\vartheta) \right]. \qquad (21c)$$

Here, the width of each side of the depletion region is given by

$$w_{Dp}, w_{Dn} = \frac{w_D}{1 + \left(\frac{N_A}{N_D} \right)^{\pm 1}} \qquad (22)$$

where w_D is computed with (18) and where the $+$ sign stands for w_{Dp} and the $-$ sign stands for w_{Dn}. The width of the top and bottom regions, for each side, that is $w_{Dn,(t,b)}$ and $w_{Dp,(t,b)}$ are computed the same way except that the relative permittivity to be used in (18) is ϵ_{clad} for the top part and ϵ_{BOX} for the bottom part.

The model for the diode is completed by the series resistances of the P and N side [31]

$$R_{p,n} = \frac{w_{pn} - w_{rib}}{2qN_{A,D}\mu_{p,n}h_{slab}L} + \frac{w_{rib}/2 \pm x_{offset} - w_{Dp,n}}{qN_{A,D}\mu_{p,n}h_{rib}L} \qquad (23)$$

where $\mu_{p,n}$ is the holes/electrons mobility [36], the $+$ sign is for R_p and $-$ for R_n, and L is the total length of the diode.

APPENDIX II
ANALYTICAL SOLUTION OF THE FREDHOLM INTEGRAL EQUATION OF THE SECOND KIND

For the problem at hand, we use the technique of successive substitution. For simplicity, we rewrite (11) as

$$T(t) = f(t) + \nu \int_a^b \mathbf{K}(t, \xi) \cdot T(\xi) d\xi \qquad (24)$$

where T is the time-dependent transfer coefficient and $\nu = 1$. The main idea is to develop the final solution by

replacing T inside the integrand by the right-hand side of (24) to obtain, after rearrangement

$$T(t) = f(t) + \nu \int_a^b \mathbf{K}\,(t, \xi) \cdot T(\xi)\mathrm{d}\xi + \\ \nu^2 \int_a^b \mathbf{K}_2\,(t, \xi) \cdot T(\xi)\mathrm{d}\xi \tag{25}$$

where $\mathbf{K}_2$ is defined as

$$\mathbf{K}_2\,(t, \xi) = \int_a^b \mathbf{K}(t, \chi) \cdot \mathbf{K}(\chi, \xi)\mathrm{d}\chi \;. \tag{26}$$

In fact, the successive substitution leads to the general form

$$T(t) = f(t) + \sum_{m=1}^n \nu^m \left(\int_a^b \mathbf{K}_m\,(t, \xi) \cdot f(\xi)\mathrm{d}\xi \right) + \\ \nu^{n+1} \int_a^b \mathbf{K}_{n+1}(t, \xi) \cdot T(\xi)\mathrm{d}\xi \tag{27}$$

where the *iterated kernel* is defined as

$$\mathbf{K}_m(t, \xi) = \int_a^b \mathbf{K}_{m-1}(t, \chi) \cdot \mathbf{K}(\chi, \xi)\mathrm{d}\chi \;. \tag{28}$$

Of course, according to this method, we have $\mathbf{K}_1(t, \xi) = \mathbf{K}(t, \xi)$. Fortunately, when $\mathbf{K}_m(t, \xi)$ is bounded in the integration domain, which is the case here, (27) converges absolutely and uniformly to the continuous limit function, i.e.

$$T(t) = f(t) + \sum_{m=1}^\infty \nu^{m-1} \left(\int_a^b \mathbf{K}_m(t, \xi) \cdot f(\xi)\mathrm{d}\xi \right) \;. \tag{29}$$

The final solutions are then readily constructed from (29).

ACKNOWLEDGMENT

REFERENCES

[1] G. L. et al., "Ring resonator modulators in silicon for interchip photonic links," *IEEE Journal of Selected Topics in Quantum Electronics*, vol. 19, no. 6, p. 3401819, 2013.

[2] P. Dong, C. Xie, L. L. Buhl, and Y.-K. Chen, "Silicon microring modulators for advanced modulation formats," in *Optical Fiber Communication Conference/National Fiber Optic Engineers Conference 2013*. Optical Society of America, 2013, p. OW4J.2.

[3] H. A. Haus, *Waves and fields in optoelectronics*. Prentice-Hall Englewood Cliffs, NJ, 1984.

[4] H. Yu *et al.*, "Trade-off between optical modulation amplitude and modulation bandwidth of silion micro-ring modulators," *Optics Express*, vol. 22, no. 12, 2014.

[5] W. D. Sacher and J. K. S. Poon, "Dynamics of microring resonator modulators," *Optics Express*, vol. 16, no. 20, p. 15741, Sep 2008.

[6] J. F. Pond *et al.*, "A complete design flow for silicon photonics," in *SPIE Photonics Europe*, 2014.

[7] F. Y. Gardes *et al.*, "40 Gb/s silicon photonics modulator for TE and TM polarizations," *Optics Express*, vol. 19, no. 12, p. 11804 – 11814, Jun 2011.

[8] H. Yu *et al.*, "Performance tradeoff between lateral and inter-digitated doping patterns for high speed carrier-depletion based silicon modulators," *Optics Express*, vol. 20, no. 12, p. 12926 – 12938, May 2012.

[9] W. L. Shockley, "The theory of *p-n* junctions in semiconductors and *p-n* junction transistors," *Bell Sys. Tech. J.*, vol. 28, no. 3, pp. 435 – 489, Jul 1949.

[10] L. O. Chua and C.-C. Chang, "High-speed non-linear circuit models for *p-n* junction diodes," *Int. J. of Circ. Theory and Applications*, vol. 16, no. 2, pp. 157 – 190, Apr 1988.

[11] M. S. Tyagi and R. Van Overstraeten, "Minority carrier recombination in heavily-doped silicon," *Solid-State Electron.*, vol. 26, no. 6, pp. 577 – 597, 1983.

[12] D. K. Schroder, "Carrier lifetimes in silicon," *IEEE Trans. Electron Devices*, vol. 44, no. 1, pp. 160 – 170, 1997.

[13] W. Bogaerts *et al.*, "Silicon micrirong resonators," *Laser & Photonics Rev.*, vol. 6, no. 1, pp. 47 – 73, Jan 2012.

[14] Z. Y. Li *et al.*, "Silicon waveguide modulator based on carrier depletion in periodically interleaved PN junctions," *Optics Express*, vol. 17, no. 18, pp. 15947 – 15958, Aug 2009.

[15] B. G. Streetman, *Solid State Electronic Devices*. Prentice Hall, 1990.

[16] R. B. Darling, "A full dynamic model for pn-Junction diode switching transients," *IEEE Trans. on Electron Devices*, vol. 42, no. 5, pp. 969 – 976, May 1995.

[17] H. Jayatilleka, W. D. Sacher, and J. K. S. Poon, "Analytical model and fringing-field parasitics of carrier-depletion silicon-on-insulator optical modulation diodes," *IEEE Photonics Journal*, vol. 5, no. 1, p. 2200211, Feb 2013.

[18] L. Chrostowski and M. Hochberg, *Silicon Photonics Design*. Cambridge University Press, 2015, ISBN: 9781107085459.

[19] H. Kogelnik, *Topics in Applied Physics*. Springer-Verlag, 1975, vol. 7, chap. 2.

[20] G. Painchaud-April, "Cavités diélectriques, formalisme de diffusion et applications," Ph.D. dissertation, Université Laval, 2013, Relevant chapters are available in english.

[21] D. Gagnon, "Modélisation ondulatoire de structures optiques résonantes," Master's thesis, Université Laval, 2011, application aux microcavités diélectriques bidimensionnelles.

[22] R. A. Soref and B. R. Bennett, "Electrooptical effects in silicon," *IEEE J. of Quantum Electronics*, vol. 23, no. 1, pp. 123 – 129, Jan 1987.

[23] M. Van Exter and D. Grischkowsky, "Carrier dynamics of electrons and holes in moderately doped silicon," *Physical Review B*, vol. 47, no. 17, pp. 12 140 – 12 149, 1990.

[24] A. Yariv, "Universal relations for coupling of optical power between microresonators and dielectric waveguide," *Elec. Lett.*, vol. 36, pp. 321–322, 2000.

[25] T. A. Burton, *Volterra integral and differential equations*. Academic Press, 1983.

[26] "IME A*STAR *(MPW services)*," [Online]. Available: https://www.a-star.edu.sg/ime/SERVICES/silicon_photonics.aspx, Accessed: 2015-01-30.

[27] W. Bogaerts *et al.*, "Compact wavelength-selective functions in silicon-on-insulator photonics wires," *IEEE Journal of Selected Topics in Quantum Electronics*, vol. 12, no. 6, pp. 1394–1401, Nov 2006.

14

[28] A. Chen and E. J. Murphy, *Broadband Optical Modulators, Science, Technology, and Applications*. CRC Press, 2012.

[29] R. Dubé-Demers *et al.*, "Analytical modeling for ultra-high-speed microring modulators with electrical and optical dynamics," in *European Conference on Optical Communications (ECOC 2014, P.2.16)*, 2014.

[30] J. Müller *et al.*, "Optical Peaking Enhancement in High-Speed Ring Modulators," *Sci. Rep.*, vol. 4, no. 6310, Aug 2014.

[31] S. M. Sze, *Semiconductor Devices: Physics and Technology*. Wiley, 2008.

[32] A. E. H. Love, "Some electrostatic distributions in two dimensions," *Proc. Lond. Math. Soc.*, vol. s2-22, no. 1, pp. 337 – 369, Jan 1924.

[33] H. B. Palmer, "The capacitance of a parallel-plate capacitor by the schwartz-christoffel transformation," *Trans. Amer. Inst. Elect. Eng.*, vol. 56, no. 3, pp. 363 – 366, 1937.

[34] R. N. Simons, *Coplanar Waveguide Circuits, Components, and Systems*, ser. Wiley Series in Microwave and Optical Engineering. John Wiley & Sons, Inc., Mar 2001.

[35] M. Abramowitz and I. A. Stegun, *Handbook of Mathematical Functions*. Dover Publications, 1965.

[36] G. Masetti, M. Severi, and S. Solmi, "Modeling of carrier mobility against carrier concentration in arsenic-, phosphorus-, and boron-doped silicon," *IEEE Trans. on Electron Devices*, vol. 30, no. 7, pp. 764 –769, Jul 1983.

[37] W. Shi, H. Yun, W. Zhang, C. Lin, T. K. Chang Y. Wang, N. A. F. Jaeger, and L. Chrostowski, "Ultra-compact, high-Q silicon microdisk reflectors," *Optics express*, vol. 20, no. 20, pp. 21840–21846, 2012.

Raphaël Dubé-Demers received the B.A. Sc. degree in physics from Université Laval, Canada, in 2012. He joined the COPL at Université Laval where he worked to obtain M.A. Sc. degree in electrical engineering and now works towards a Ph.D. degree in electrical engineering. In the photonics group he specialized in the modeling, development and testing of resonant SOI modulators. His research interests also include numerical analysis and integrated coherent transmission systems.

Jonathan St-Yves received the B. Eng. degree in engineering physics from Université Laval, Canada in 2014. He is working towards the M.A. Sc. degree in electrical engineering at Université Laval. His research interests are in silicon photonics and optical communications, focused towards integrated optical filters and detectors.

Antoine Bois received the B.Eng. in electrical engineering from Université Laval in 2015. He is a student member of the Optical Society of America (OSA). Research interests include silicon photonics and, more broadly, nanophotonics.

Qiuhang Zhong is a Ph.D. candidate at the department of electrical and computer engineering at McGill University.

Michael Caverley received the B.A.Sc degree in engineering physics from the University of British Columbia, Vancouver, BC, Canada, in 2013. He is currently working towards the M.A.Sc degree in electrical and computer engineering at the University of British Columbia. His research interests include high-speed silicon modulators and silicon microring-based filters for dense wavelength-division multiplexing applications.

Yun Wang is a Ph.D. student at University of British Columbia in the department of Electrical and Computer Engineering. He received his B.A. degree in optoelectronic engineering from Shenzhen University, China, in 2011, and received his Master of Applied Science degree in May 2013 from University of British Columbia. His mastes thesis is on grating coupler designs based on the silicon-on-insulator platform. His current research interests are in the sub-wavelength grating designs and the integration of III-V lasers with silicon photonics chips. He is a student member of the IEEE, OSA and is the president of the SPIE student chapter at UBC.

Lukas Chrostowski is an Associate Professor of Electrical and Computer Engineering at the University of British Columbia, Vancouver, BC, Canada. He earned the B.Eng. in electrical engineering from McGill University in 1998 and a PhD from the University of California at Berkeley in 2004. Chrostowski received the Killam Teaching Prize at the University of British Columbia in 2014. He co-authored the book Silicon Photonics Design (Cambridge University Press, 2015). He is the Program Director of the NSERC CREATE Silicon Electronic-Photonic Integrated Circuits (SiEPIC) training program in Canada, and has been teaching silicon photonics workshops and courses since 2008. He has published over 170 journal papers and conference proceedings. His research interests are in silicon photonics, semiconductor lasers, optical communications and bio-photonics.

Sophie LaRochelle (M'00) received a Bachelor's degree in engineering physics from Université Laval, Canada, in 1987; and a Ph.D. degree in optics from the University of Arizona, USA, in 1992. From 1992 to 1996, she was a Research Scientist at the Defense Research and Development Canada - Valcartier, where she worked on electro-optical systems. She is now a professor at the Department of Electrical and Computer Engineering, Université Laval, where she holds a Canada Research Chair (Tier 1) in Advanced Photonics Technologies for Communications. Her current research activities are focused on active and passive components for optical communication systems including silicon photonic devices, Bragg gratings filters, multi-wavelength and pulsed fiber lasers. Other research interests include optical fibers and amplifiers for spatial division multiplexing, all-optical signal processing and routing, and transmission of radio-over-fiber signals including UWB and GPS. Dr. LaRochelle is an IEEE senior member and an OSA Fellow.

David V. Plant (F'07) received the Ph.D. degree from Brown University, Providence, RI, USA, in 1989. He was a Research Engineer at the University of California Los Angeles from 1989 to 1993, and has been a Professor at McGill University since 1993, where he holds a James McGill Professorship. He has published more than 400 journal and conference papers and has one licensed patent. He has received five teaching awards and numerous other awards including the IEEE Photonics Society Distinguished Lectureship and the IEEE Microwave Theory and Techniques Society Microwave Prize. He is a Fellow of OSA, Engineering Institute of Canada, and the Canadian Academy of Engineering. He currently holds a Killam Research Fellowship.

Wei Shi is an Assistant Professor with the Department of Electrical and Computer Engineering, Université Laval. He received the PhD degree in electrical and computer engineering from the University of British Columbia,Vancouver in 2012. During his PhD, he received many awards and scholarships including the BCIC Innovation Scholarship. Before joining Université Laval in 2013, he was a researcher at McGill University, where he held an NSERC postdoctoral fellowship. His research interests include silicon photonics and integrated electronic-photonic systems for high-capacity optical transmissions.